Plasma Motion inside Flaring Regions Revealed by Doppler Shift Information from *SDO/EVE* Observations

Zhixun Cheng[1,2] , Yuming Wang[1,2] , Rui Liu[1,2] , Zhenjun Zhou[2,3] , and Kai Liu[1,2]
[1] School of Earth and Space Sciences, University of Science and Technology of China, Hefei 230026, People's Republic of China; ymwang@ustc.edu.cn
[2] CAS Center for Excellence in Comparative Planetology, Hefei 230026, People's Republic of China
[3] School of Atmospheric Sciences, Sun Yat-sen University, Zhuhai, Guangdong 519000, People's Republic of China

Abstract

Plasma motions within flaring regions provide key information for us to understand the flare processes. Here, we study two X-class flares near the solar disk center, one on 2014 January 7 and the other on 2012 March 7, by using 10 extreme ultraviolet (EUV) emission lines from the *Solar Dynamics Observatory*/EUV Variability Experiment (EVE). The EVE plasma dynamic spectrum chart, a 2D map of Doppler shift against temperature and time, is constructed based on a spectroscopic analysis of the EUV lines. Three kinds of plasma motion are identified in the plasma dynamic spectrum charts: chromospheric evaporation (100–200 km s^{-1}) above 1 MK, cooling inside post-flare loops (approximately 150 km s^{-1}) between 0.3 and 1 MK, and condensation at footpoints ($<$30 km s^{-1}) below 0.3 MK. We find that the chromospheric evaporation and condensation at footpoints started in the impulsive phase almost simultaneously, while the cooling occurred later in the gradual phase, with a time delay of more than 10 minutes, probably implying the timescale of evaporation movement and heat loss. Atmospheric Imaging Assembly observations and differential emission measure (DEM) analyses suggest that the cooled plasma moves downward within the cold transition region (TR) loops, from top to feet, which are below the hot coronal loops. Besides, the reversal temperature between blue/redshifts is close to 1 MK, implying that the boundary of upflowing/downflowing plasma is located at the lower corona or the upper TR.

Key words: line: profiles – Sun: corona – Sun: flares – Sun: UV radiation

1. Introduction

During a flare, released magnetic energy is transformed into radiation, energetic particles, heated plasma, waves, etc. (e.g., Hudson et al. 2011). The radiative output represents a substantial fraction of the flare energy (Emslie et al. 2012), most of which appears in extreme ultraviolet (EUV) passband, from 10 to 120 nm (Fröhlich & Lean 2004). Although EUV emission contributes a small fraction of solar total irradiance, the majority of the Sun's variability is reflected in the EUV output (Woods et al. 2006; Moore et al. 2014). As the EUV spectral range is a main observation window of solar flares, the Doppler shift of EUV emission lines can reveal various dynamic processes of plasma during flares.

In the standard solar flare model, magnetic reconnection occurs in the corona and releases a large amount of energy (Priest & Forbes 2001). The released energy drives nonthermal particles and thermal conduction downward to the lower atmosphere and further generates hard X-ray emissions at the top and feet of flare loops. The energy that deposits in the dense chromosphere heats up the local plasma, which evaporates into the corona subsequently due to pressure imbalance (Neupert 1968; Hirayama 1974; Acton et al. 1982). The evaporation then fills hot coronal loops, which can be observed as post-flare loops in soft X-ray and EUV passbands. Chromospheric evaporation was often detected as blueshift in hot coronal lines, the upward velocity of which may reach tens to hundreds of km s^{-1} (e.g., Teriaca et al. 2003, 2006; Brosius & Phillips 2004). Many instruments have detected such blueshifts in different coronal lines and reveal the temperature feature of the evaporation. Previous studies reported blueshifts in Fe XIX and Fe XXI emission lines at temperatures of about 10 MK using the *Solar and Heliospheric Observatory* (*SOHO*)/

Coronal Diagnostic Spectrometer and IRIS, respectively (e.g., Del Zanna et al. 2006; Graham & Cauzzi 2015). Li et al. (2015) studied the blueshift of a hotter coronal line, Fe XXIII at 13 MK, by using the EUV Imaging Spectrometer (EIS) aboard *Hinode*. What is more, Hudson et al. (2011) found that the Fe XXIV line from the *Solar Dynamics Observatory* (*SDO*)/EUV Variability Experiment (EVE) presents decreasing apparent blueshifts as expected from chromospheric evaporation flows during several flare events, which has a super-high temperature of 16 MK.

As the heated plasma evaporates into the corona, some cold materials move downward in the transition region (TR) and chromosphere. There are two probable mechanisms to interpret such cold downflows: (1) evaporated plasma in the loops fall back to the chromosphere because of gravity, after a cooling process involved with heat conduction and radiative losses. The downflows move within the cooler loops that are formed from the hotter loops and are located below them (e.g., Schmieder et al. 1995; Bradshaw & Cargill 2005). (2) During explosive chromospheric evaporation, rapid heating produces an enhanced pressure at footpoints and drives downward-moving cool and dense chromospheric condensations, besides the evaporation, due to momentum balance (Fisher et al. 1985). Slight redshifts corresponding to downward velocities of tens of km s^{-1} have also been found in chromospheric and TR lines, which are thought to be observational evidence of thermal condensation (e.g., Teriaca et al. 2003, 2006; Kamio et al. 2005; Del Zanna et al. 2006). Some studies focused on where the reversal between hot upflows in evaporation and cold downflows in cooling or condensation occurs in the solar atmosphere. Different flow reversal temperatures would imply different energy deposition heights, rates, or duration driven by magnetic reconnection during flares (Liu et al. 2009). Evaporation models predict that the reversal temperature is

below 1 MK (Fisher et al. 1985), which is consistent with the observational studies by Kamio et al. (2005) and Del Zanna et al. (2006). However, higher reversal temperatures, such as 2 MK, or even 5 MK, were also suggested (Milligan 2008; Li & Ding 2011).

SDO/EVE provides global observations with high resolutions in both time and spectrum, though it has no spatial resolution. In our previous work, EVE data have been used to construct thermodynamic spectrum charts, a 2D image of emission line intensity against temperature and time (Wang et al. 2016, hereafter Paper I). Such charts provide a comprehensive view of thermodynamic processes during solar flares compared with the spectral analysis of a single emission line. EVE data not only contain the information of the intensity of emission lines, but also the information of Doppler shifts, which may reveal dynamic processes and are not included in thermodynamic spectrum charts yet. Thus, here we analyze the Doppler shift information contained in the EVE spectral data during solar flares and try to construct 2D EVE plasma dynamic spectrum charts based on the Doppler shift analysis.

Since EVE receives EUV spectra of the whole visible Sun without spatial resolution, the Doppler shift derived from EVE data actually contain a global effect of plasma motion on the entire solar disk, whereas we are focusing on localized dynamic processes in flaring regions. However, considering the fact that flare EUV emission accounts for the major varying component of the total EUV irradiance from the Sun, the Doppler shift from EVE observation can substantially represent the motion of matter in flare loops, especially during those violent eruptions without other simultaneous events. In addition, it is known that only the motion of emission source along the line of sight can lead to a shift in the wavelength. Thus, we select two X-class flares occurring near the disk center—one on 2014 January 7 and the other on 2012 March 7— to perform our Doppler shift analysis. The aforementioned dynamic processes, i.e., hot upflows in chromospheric evaporation and cold downflows in cooling/condensation, are studied by investigating the two flares. The physics behind the revealed Doppler shift features are also discussed.

2. Data and Method

Detailed descriptions of EVE instruments and data can be found in some previous papers (e.g., Hudson et al. 2011; Woods et al. 2012). Briefly, the Multiple EUV Grating Spectrograph (MEGS), one of EVE's subsystems, measures the spectral irradiance from 5 to 105 nm, with a pixel size of 0.02 nm in its wavelength and a cadence of 10 s. MEGS has four detection channels: MEGS-A, MEGS-B, MEGS-SAM, and MEGS-P. Our study uses data from MEGS-A and MEGS-B, with wavelengths spanning 5–37 nm and 35–105 nm. MEGS-A worked continuously, whereas MEGS-B operated intermittently. Seven emission lines from MEGS-A and three emission lines from MEGS-B were used in the following Doppler shift analysis. Table 1 lists the 10 emission lines as well as their corresponding peak-response temperatures.

The Doppler shift information of a specific emission line can be extracted from its emission profile as shown in the example in Figure 1, which displays the irradiance around wavelength 33.54 nm, i.e., the Fe XVI emission line, at 16:00:05 UT on 2010 November 5. Since the EUV emission line is contaminated with continuum emission, we use a Gaussian plus linear function to fit the total emission and treat the Gaussian

Table 1
Emission Lines Provided by MEGS

No.	Ions	Wavelength (nm)	log T (K)	Channels
1	Fe XVIII	9.39	6.81	MEGS-A
2	Fe XVI	33.54	6.43	MEGS-A
3	Fe XV	28.42	6.30	MEGS-A
4	Fe XII	19.51	6.13	MEGS-A
5	Fe XI	18.04	6.07	MEGS-A
6	Fe IX	17.11	5.81	MEGS-A
7	Fe VIII	13.09	5.57	MEGS-A
8	O VI	103.19	5.47	MEGS-B
9	O V	62.97	5.37	MEGS-B
10	C III	97.70	4.84	MEGS-B

fitting curve as the irradiance from the emission line of interest. To reduce possible contamination from neighboring lines, only the data points between the two minima at two sides of the line peak are selected for the fitting. The central wavelength corresponding to the Gaussian fitting curve is then used to calculate the Doppler shift away from the reference wavelength of the emission line. Besides, we use multiple-Gaussian distribution to fit the line profiles to check the reliability of our single-Gaussian fitting method. It turns out that there is no significant difference in determining the value of fitted central wavelength. Since a single-Gaussian fitting has less free parameters and therefore is more robust than multi-Gaussian fitting, we decide to use a single-Gaussian fitting in this study.

There are two methods to determine the reference wavelength. One is to read it from some atomic database, e.g., CHIANTI (version 6.0.1, Dere et al. 1997, 2009). But by applying the reference wavelengths from the CHIANTI database in our study, we find that the calculated Doppler shifts of the most selected lines are systematically redshifted, corresponding to about 20 km s^{-1} on average, during a quiet period of the Sun. Such slight deviations may be attributed to the so-called background Doppler error due to solar rotation, orbital motion of *SDO*, and an inherent error of the instrument, as first pointed out by Hudson et al. (2011) and could also possibly be caused by systematic steady flows of plasma in the quiet Sun. No matter which is the main reason, we need to deduct such deviations from observations to obtain the Doppler shifts purely caused by a flare. Thus, here we use the second method to determine the reference wavelength, just like what Hudson et al. (2011) did. In this method, we set the reference wavelength of a certain emission line to be the median value of the fitted central wavelengths within 60 minutes prior to the flare onset, which may effectively eliminate the background Doppler error. When the emission line was not observed before a flare, we use the median value of the fitted central wavelength when or after the flare is fading away as the reference wavelength.

However, in our selected 10 spectral lines, there is 1 line, Fe XVIII 9.39 nm, that we cannot find its reference wavelength based on the second method due to the blending by neighboring lines. As shown in Figure 2, the CHIANTI database provides simulation results of solar EUV line profiles at different temperatures by using an isothermal model, and suggests that Fe XVIII 9.39 nm, a hot coronal line, is not present before or after flares. In the condition of log $T < 6.3$, i.e., in the quiet corona, the line profile around 9.39 nm is dominated by another cold line, Fe X 9.40 nm, so we cannot obtain the
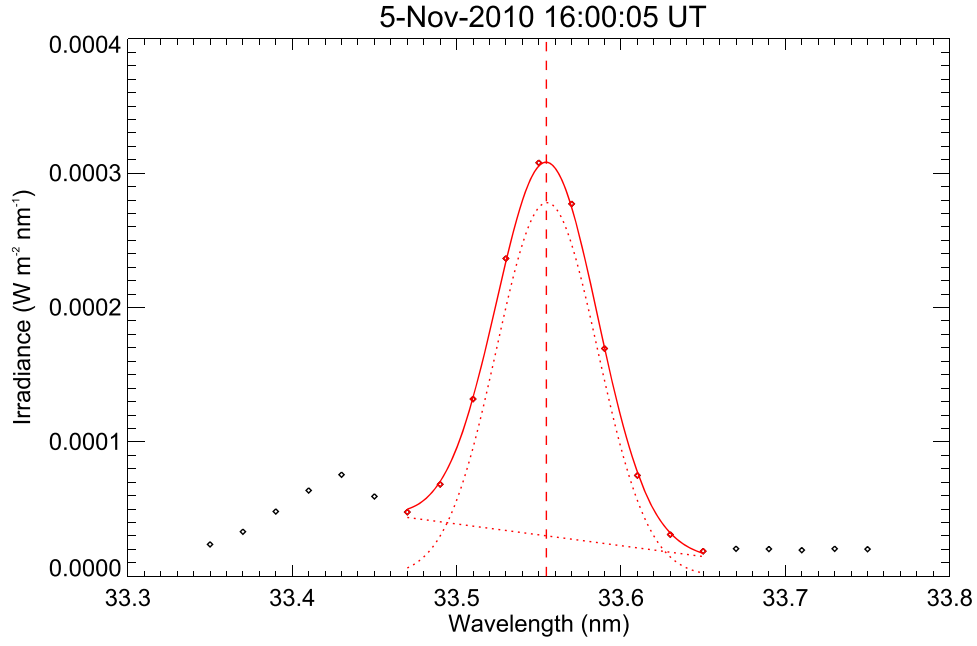
Figure 1. Example showing the EVE line profile around Fe XVI 33.54 nm. The red diamonds are used in our fitting procedure. The solid curve is the fitting results, consisting of a Gaussuan component and a linear component denoted by the dotted lines. The red vertical dashed line is the fitted central wavelength.
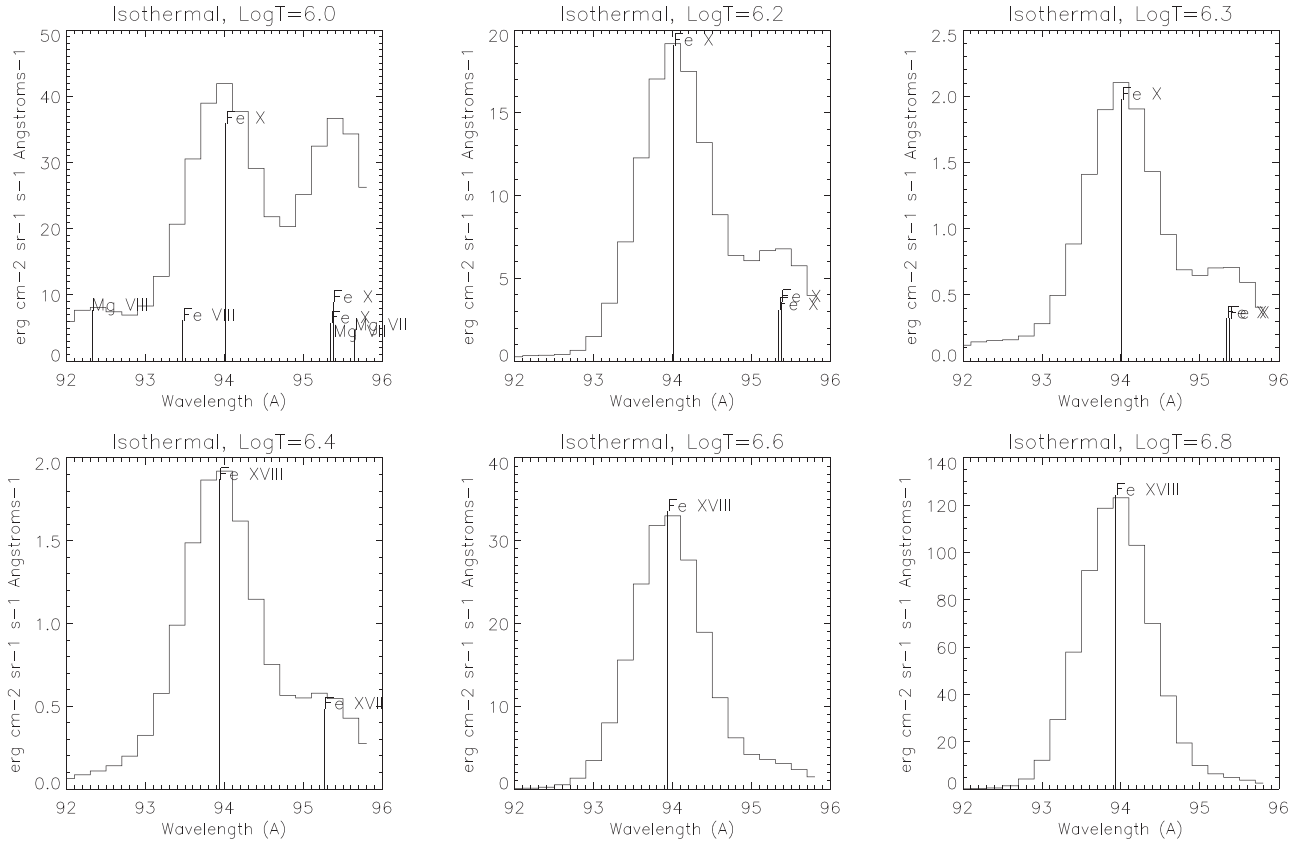

Figure 2. CHIANTI simulations of the emission line profile around Fe XVIII 9.39 nm, at log T = 6.0, 6.2, 6.3, 6.4, 6.6, and 6.8, respectively. These simulations are based on an isothermal model.

reference wavelength of Fe XVIII 9.39 nm by investigating pre/post-flare observed wavelength. For this special line, we choose to use spectral information from the CHIANTI database to determine its reference wavelength. Considering that the maximum intensity of Fe X 9.40 nm in quiet time, less than 50 erg cm^{-2} sr^{-1} s^{-1} Å^{-1}, is about one third of that of Fe XVIII 9.39 nm during flares, reaching up to more than 120 erg cm^{-2} sr^{-1} s^{-1} Å^{-1}, we regard it as a reliable time range when the intensity of the fitted line profile around 9.39 nm increases by triple pre-flare level, suggesting that
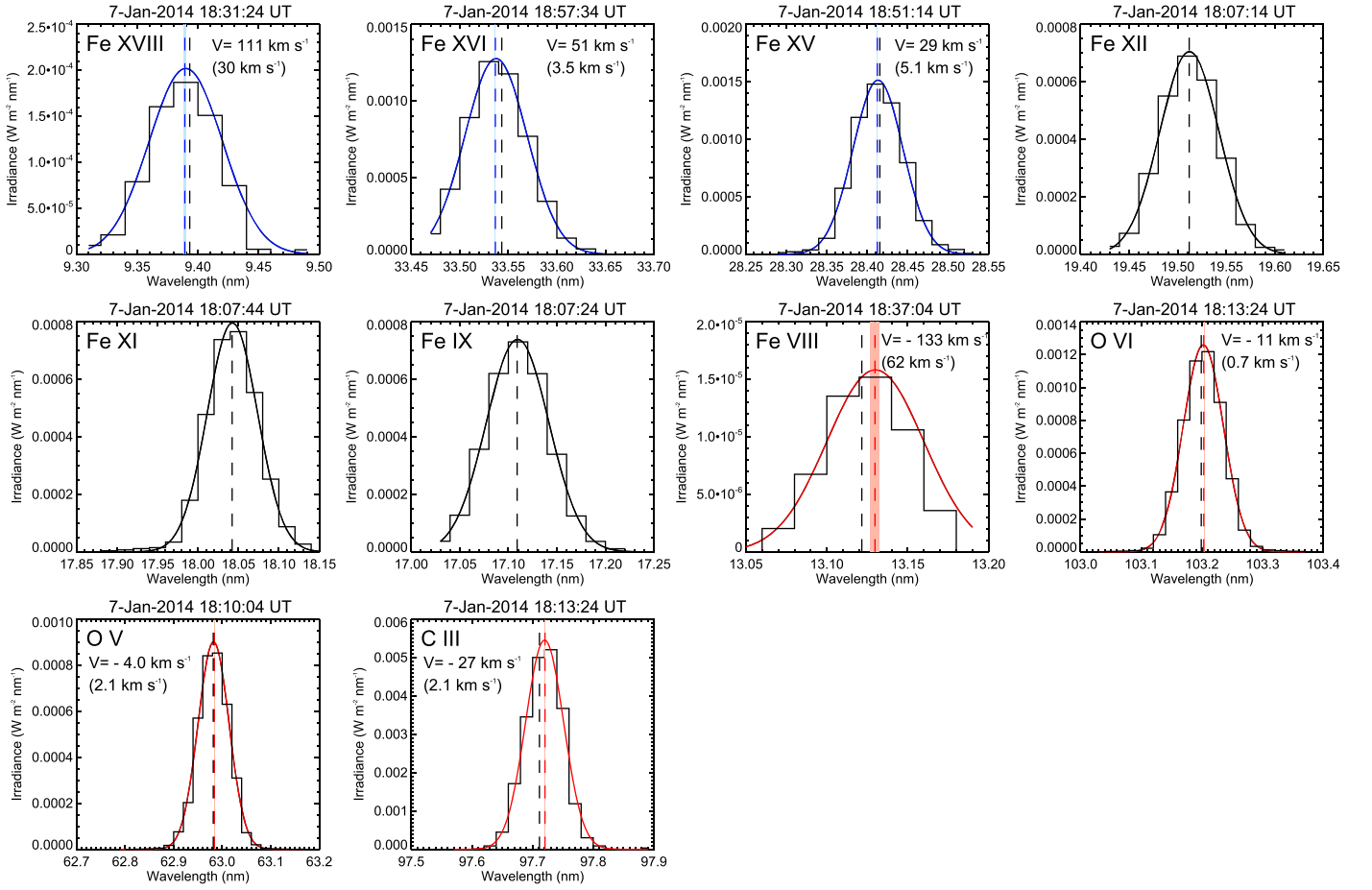
Figure 3. Example showing the profiles of the 10 emission lines after the background continuum subtraction. The red/blue solid curves correspond to the fitting results of red/blueshift. The colored dashed lines are the fitted central wavelengths, and the black dashed lines are the reference wavelengths. Shadows indicate the 1σ errors of the fitted central wavelengths. The Doppler velocities and their uncertainties are given in these panels, except for Fe XII, Fe XI, and Fe IX, where the values are not significantly different from zero. Each panel shows the profile of the emission line at the moment when its Doppler shift reached the maximum.
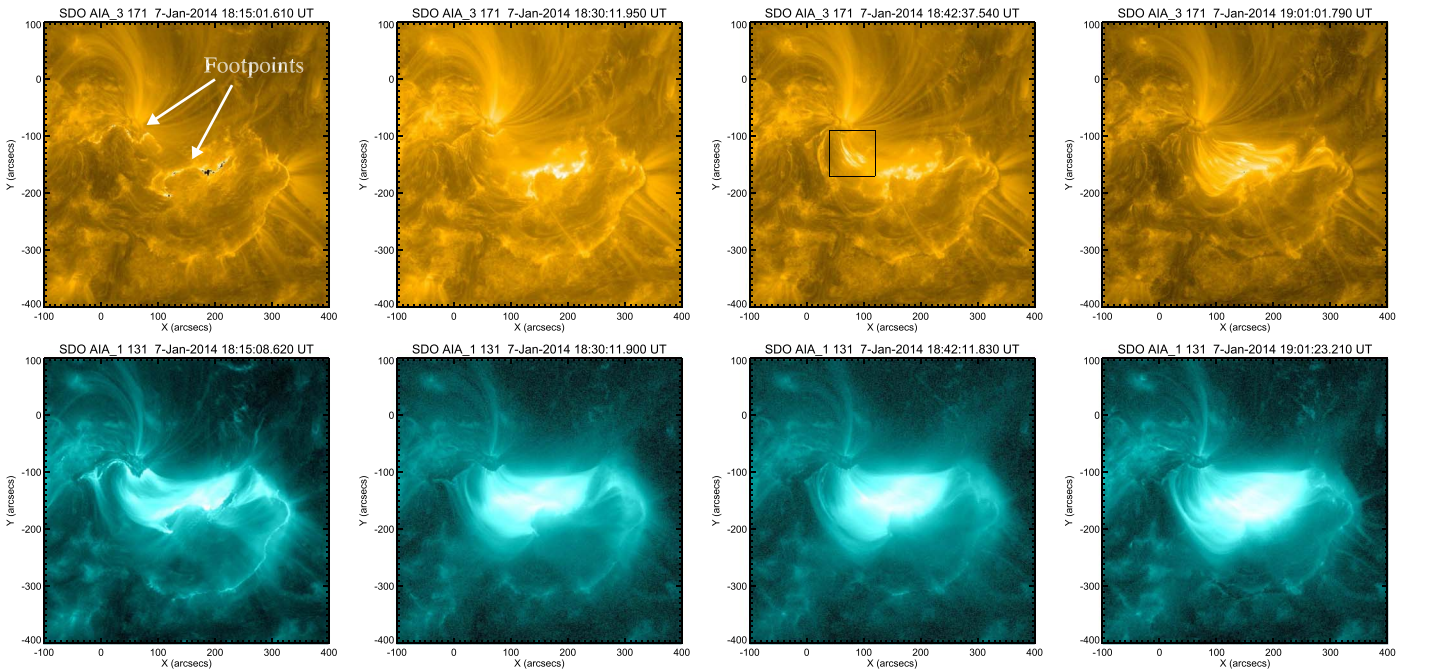

Figure 4. AIA 171 and AIA 131 images of the flare before, at, and after the flare peak (18:30 UT). The black box shows the position where the brightening of AIA 171 started.
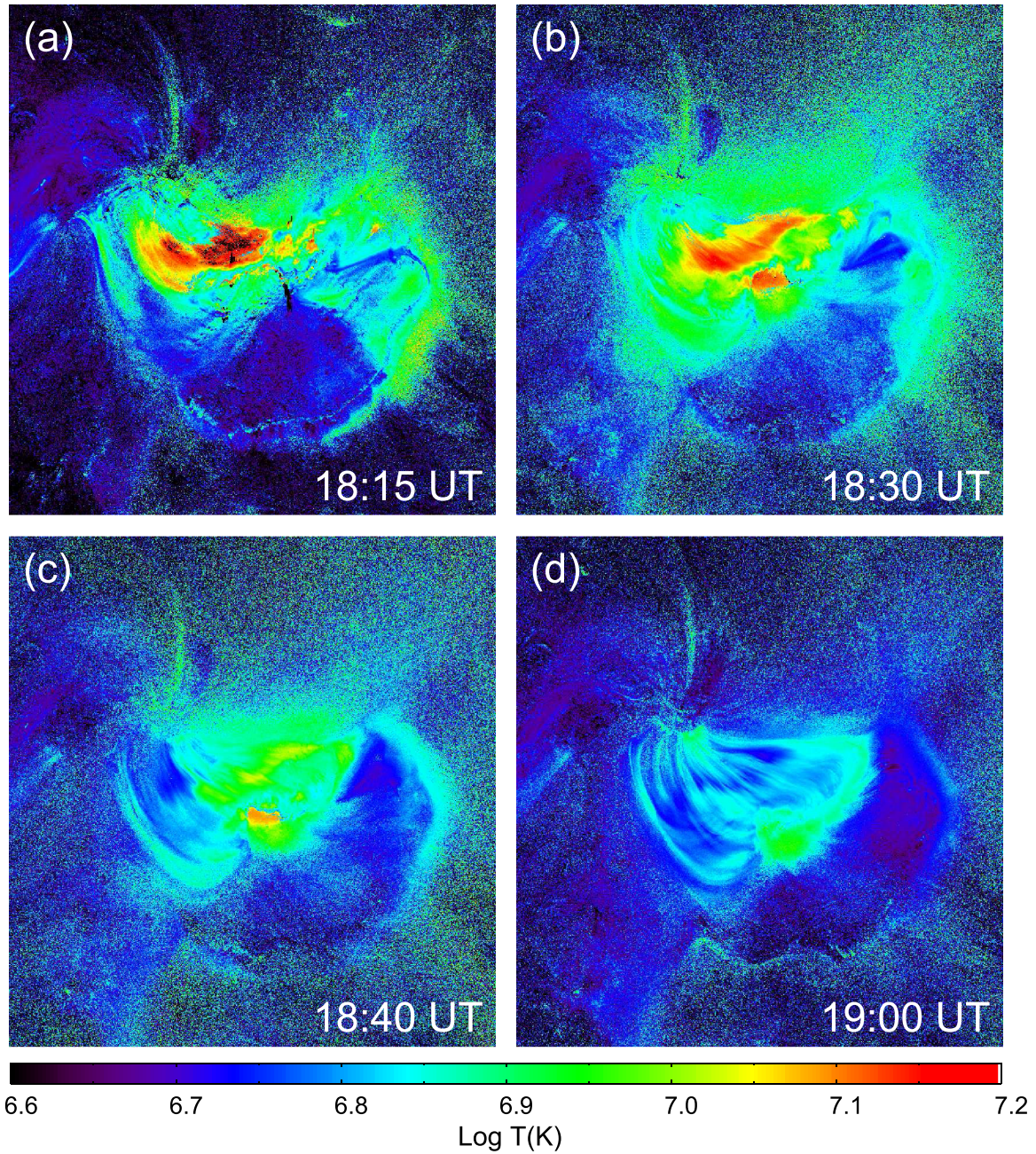
Figure 5. DEM temperature maps of the flare, showing the same region indicated by Figure 4. (a) Before the flare peak. (b) At the flare peak (18:30 UT). (c) and (d) After the flare peak. The temperature range is 4–17 MK.

Fe XVIII 9.39 nm has become dominating the line profile then. We use wavelength shift of Fe XVIII 9.39 nm in this reliable time range to calculate the Doppler velocity and ignore the data before and after it. As mentioned above, the observed wavelengths of the other emission lines during quiet time present systematic redshifts of about $20\,\mathrm{km\,s^{-1}}$, compared to the corresponding CHIANTI's wavelengths. So there might be a slight underestimation of the blueshift of Fe XVIII 9.39 nm, when we use the CHIANTI's wavelength as its reference wavelength.

We apply the above procedure to the 10 EUV emission lines to obtain the Doppler shifts as well as Doppler velocities. Figure 3 shows the exemplary line profiles after the background continuum subtraction during the X1.2 flare on 2014 January 7 as well as the Doppler velocities and uncertainties

derived from the Gaussian fitting, except for Fe IX 17.11 nm, Fe XI 18.04 nm, and Fe XII 19.51 nm (see the discussion in Section 3.1). The 1σ error of the fitted central wavelength is used to calculated the uncertainty of Doppler velocity. The uncertainties are found to be small enough compared with the absolute Doppler velocities of the emission lines, benefiting from the fact that the line profiles basically conform to a single-Gaussian distribution.

3. Observations and Results

3.1. The X1.2 Flare on 2014 January 7

Based on the *Geostationary Operational Environmental Satellite* (*GOES*) soft X-ray measurement, the flare (S09E09) started at 18:06 UT and peaked at 18:30 UT. During the same
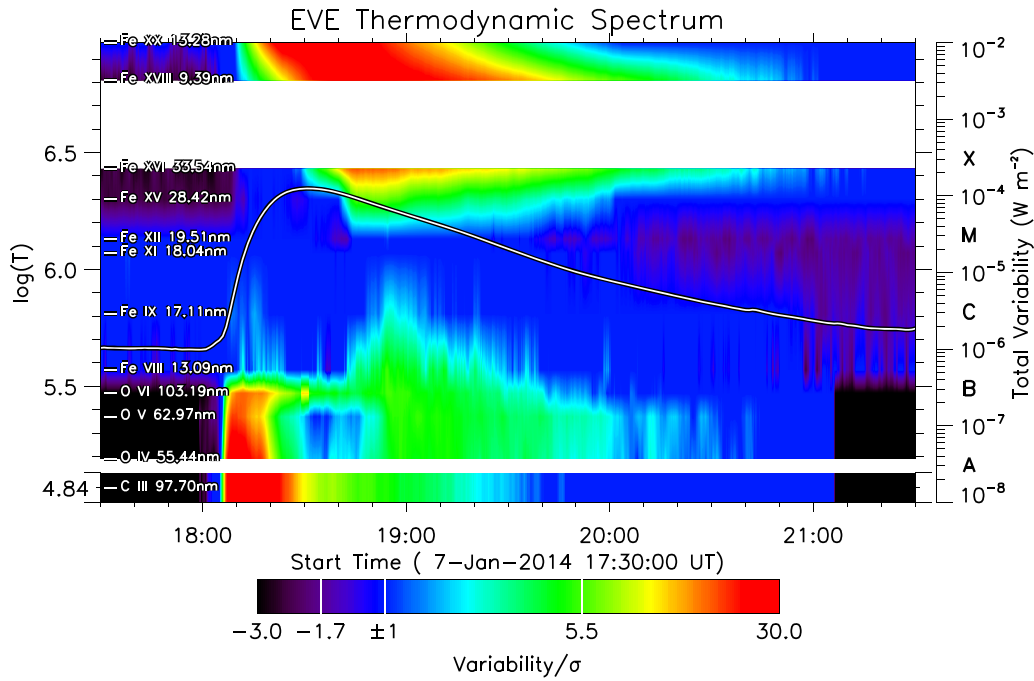
Figure 6. EVE thermodynamic spectrum chart showing the variability. The 12 emission lines used in the charts are indicated on the left. The white line is derived from the *GOES* soft X-ray with the y-axis on the right.

period, there was no other flare on the visible solar disk, and therefore the spectral features from EVE reflect the dynamic and thermodynamic processes of the flare. Figure 4 shows the *SDO*/Atmospheric Imaging Assembly (AIA) 171 and 131 images before, at, and after the peak time of the flare, displaying an evolution of the post-flare loops in the hot corona and cooler TR, respectively. It was a two-ribbon flare as can be seen in AIA 171 image at 18:15 UT. The AIA 131 passband shows the emission from a higher temperature of about 10 MK than AIA 171 passband and presents the formation of hot coronal loops connecting the two footpoints shown in AIA 171. As the flare developed, the hot loops grew and rose gradually. AIA 171 presents cool post-flare loops in the TR at about 0.63 MK. What is interesting here is that AIA 171 did not show any bright feature of cool post-flare loops until 18:42 UT, 12 minutes after the flare peak. In other words, the cool TR loops were formed apparently later than the hot coronal loops, suggesting a delayed plasma cooling inside the post-flare loops. The brightening of AIA 171 started at the top of the cool loops at 18:42 UT (shown by the black box) and then filled up the whole loops at 19:01 UT.

Further, we apply the differential emission measure (DEM, Schmelz et al. 2011; Cheng et al. 2012) method to the six AIA passbands to create temperature maps of the flare, as shown in Figure 5. The four temperature maps in the range of 4–17 MK show the temporal evolution of the thermal structures in the corona during the flare. The kernel region near the top of the hot coronal loops was found to be super hot (>15 MK) during the impulsive phase of the flare before 18:30 UT. As the hot loops grew up, the super-hot region moved with the loop top, and the peak temperature decreased from 17 to 12 MK because of a cooling process. Compared to the loop top, the legs of the hot loops were relatively cooler and were below 10 MK.

The EVE thermodynamic spectrum chart provides thermal features of the 10 EUV emission lines during the flare, which has been shown in Figure 21(a) of Paper I and is also shown

here as Figure 6 for convenience. First, the flare heated the coronal lines above 1 MK, starting at 18:10 UT, which is slightly later than the onset time of the *GOES* X-ray. The emission enhancements of the lines at high temperatures were more significant and occurred earlier than those at low temperatures. This enhancement is also used to determine when the line Fe XVIII 9.39 nm is eligible for the Doppler shift analysis. The emission of the TR lines (0.3–1.0 MK) began to enhance in the gradual phase, after a delay of about 30 minutes compared to the coronal heating, reflecting the cooling process. Besides, apparent emission enhancements of the lower TR lines below 0.3 MK were found in the impulsive phase.

To further study the dynamic processes of solar plasma at different temperatures during the flare, the Doppler velocities derived from the aforementioned 10 EUV emission lines are given in Figure 7 with positive/negative values corresponding to blue/redshift of the emission lines. The uncertainties in these velocities are indicated by shadows. Figures 7(a) and (b) show that the Doppler velocities were significantly large compared to the uncertainties during the impulsive and gradual phases of the flare. Due to the lack of MEGS-B data before the flare, the reference wavelengths of the three cold lines, i.e., O VI 103.19 nm, O V 62.97 nm, and C III 97.70 nm, are set to be the median values of the fitted central wavelengths during the terminal phase of the flare, from 20:30 UT to 21:00 UT in this case, by assuming that the plasma had reached a static state without significant mass flows after the flare faded away. For Fe XVIII 9.39 nm, the reference wavelength is determined by the CHIANTI database, and only the reliable data during the flare (18:10–20:00 UT) are retained, as we mentioned in Section 2. Notice that the Doppler velocity here is just the lower limit of the actual velocity, because we can only measure the projected component of plasma motion along the line of sight.

The Fe XVIII 9.39 nm, Fe XVI 33.54 nm, and Fe XV 28.42 nm show blueshifts, revealing the evolution of chromospheric
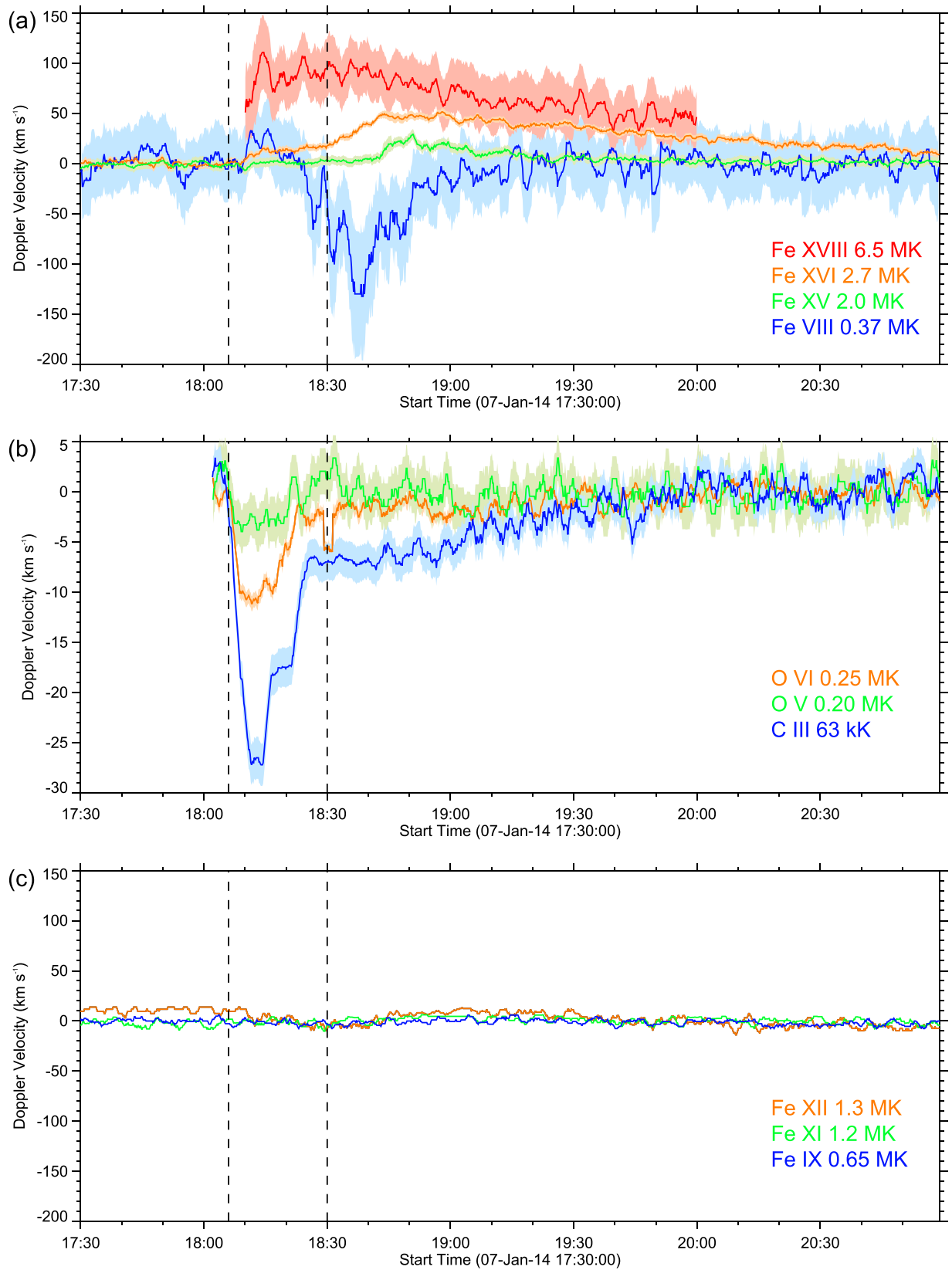
Figure 7. Doppler velocities of the 10 emission lines from MEGS-A and MEGS-B with positive/negative values corresponding to the blue/redshift. The uncertainties in the velocities are indicated by shadows, except for Fe XII, Fe XI, and Fe IX. The two vertical dashed lines show the flare onset and the flare peak.

evaporation as a decay process of its velocity and temperature. Specifically, Fe XVIII 9.39 nm at 6.5 MK reached a strong blueshift of about 100 km s^{-1} in the impulsive phase. This is

probably the reason why we see such high temperatures near the top of flare loops in the impulsive phase of the flare in Figures 5(a) and (b). The lines Fe XVI 33.54 nm at 2.7 MK and
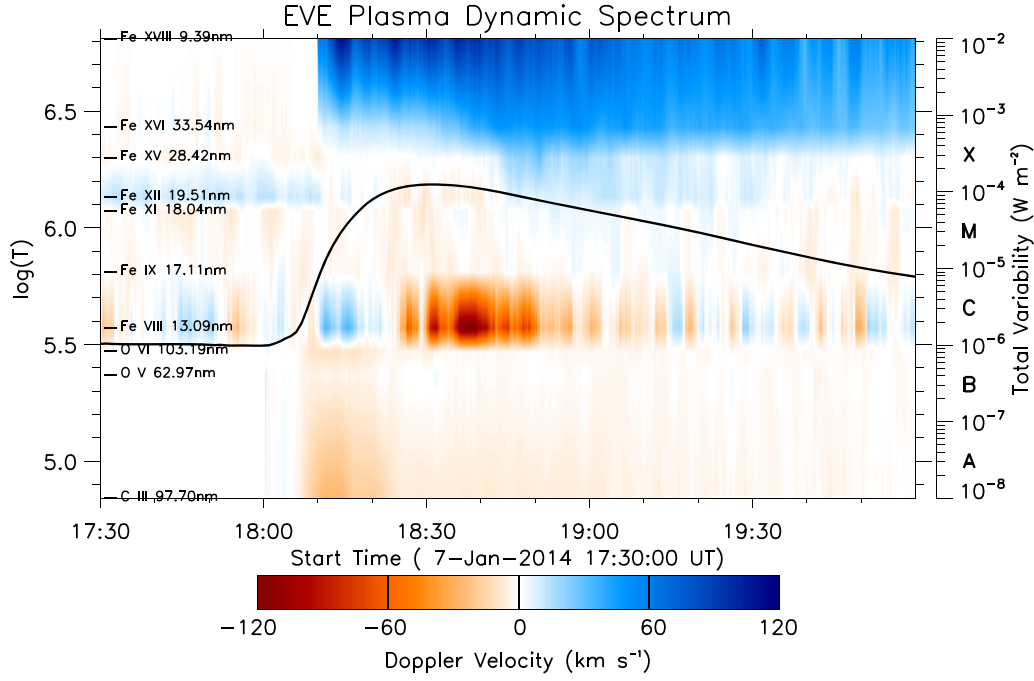
Figure 8. EVE plasma dynamic spectrum chart showing the Doppler shift. The 10 emission lines used in the chart are indicated on the left. The black line is derived from the *GOES* soft X-ray with the *y*-axis on the right.
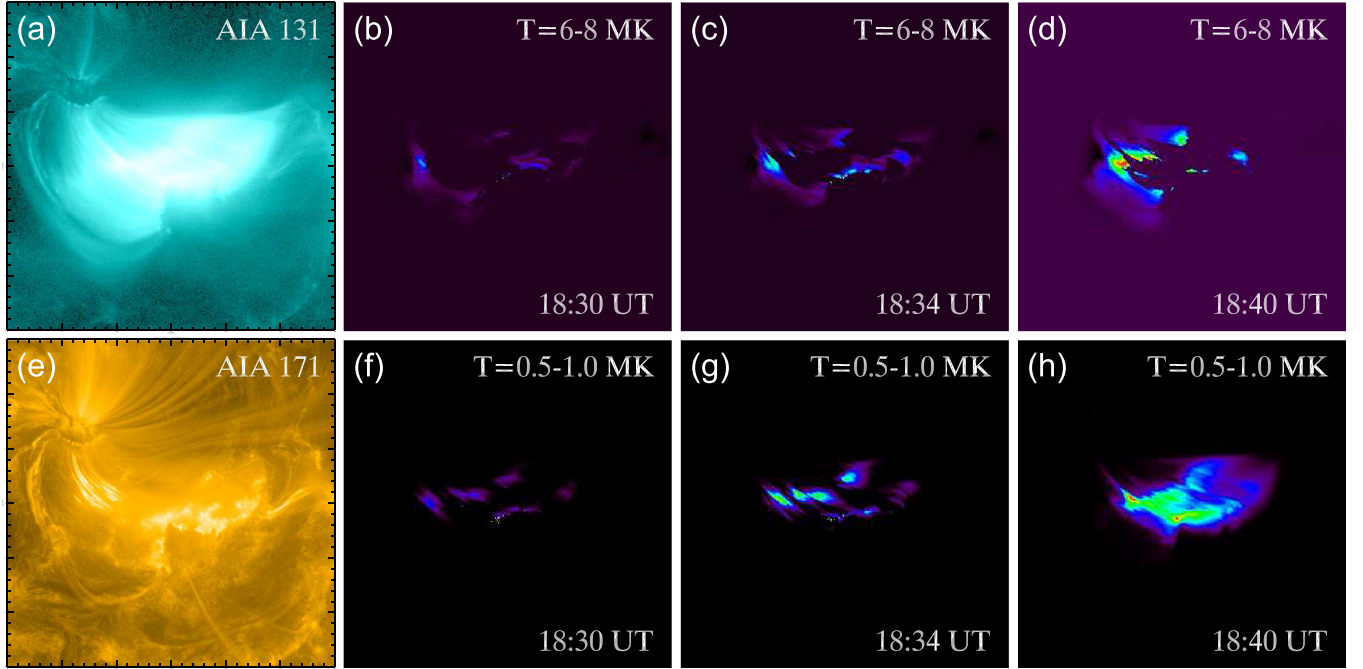

Figure 9. AIA images and emission maps from the DEM analysis. The two rows of DEM maps are in temperature bands of 6–8 and 0.5–1.0 MK, corresponding to chromospheric evaporation and cooling within post-flare loops, respectively. The images are enlarged for a clearer view, where the ranges of *x*-axis and *y*-axis are [0, 300] and [−300, 0] arcsec, respectively.

Fe XV 28.42 nm at 2.0 MK also showed slight blueshifts of 51 and 29 km s^{-1} subsequently in the gradual phase, suggesting that the chromospheric evaporation started in the impulsive phase and diminished both in the velocity and temperature as the flare developed. The chromospheric evaporation, revealed by the blueshifts of those three high-temperature lines, should be responsible for the coronal heating above 1 MK in the EVE thermodynamic spectrum chart (see Figure 6). Meanwhile, Fe VIII 13.09 nm, a TR line at 0.37 MK, presents a significant

redshift of 133 km s^{-1} in the gradual phase, after an evident delay of about 20 minutes compared to the chromospheric evaporation. In other words, a delayed motion formed by cold downflows occurred in the TR, posterior to the coronal heating. The time delay here is consistent with the AIA observation in which the cool TR loops in AIA 171 appeared apparently later than the formation of hot coronal loops in AIA 131 (see Figure 4).
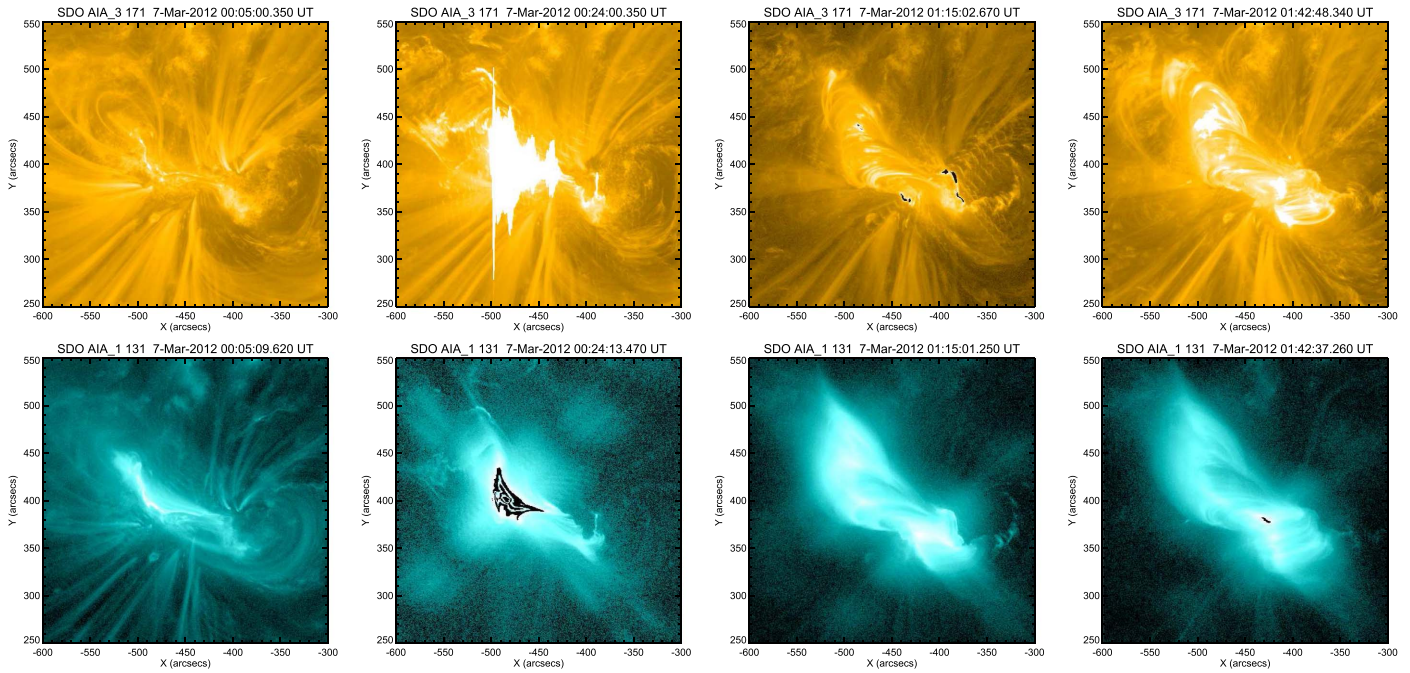
Figure 10. AIA 171 and AIA 131 images of the flare at the flare onset (00:05 UT), at the main peak (00:24 UT), and at and after the second peak (01:15 UT).

For the three cold lines, O VI, O V, and C III, slight redshifts below 30 km s^{-1} are found during the impulsive phase of the flare, almost at the same time with the evaporation. The appearance time of these redshifts is consistent with the emission enhancements of the lower TR lines below 0.3 MK in Figure 6. Such cold and slow downflows may result from the overpressure during a rapid temperature increase at footpoints, i.e., explosive evaporation (Fisher 1987). Probably because the initial rapid heating became faint, the downward plasma velocities recovered to approximately zero later in the gradual phase.

In a number of flare cases studied, we find that Fe IX 17.11 nm, Fe XI 18.04 nm, and Fe XII 19.51 nm present nearly no emission enhancement compared with other lines (see Figures 6 and 12), and their Doppler velocities just show irregular oscillations within $+/-20$ km s^{-1} during all stages of a flare. These three lower corona lines are within a narrow temperature range between 0.65 and 1.3 MK, a typical temperature of the quiet corona, and seem to be insensitive to flares. Since their line profiles are barely impacted by flares, we think that this kind of slight oscillation of Doppler velocities probably reflects the total effect of random plasma motion in the entire visible solar disk and did not make a further analysis on the characteristic of their Doppler velocities as well as the uncertainties.

Based on the above Doppler shift study on the 10 EUV emission lines at different temperatures, we then construct a 2D EVE plasma dynamic spectrum chart to provide a comprehensive view of plasma motion inside flaring regions, as shown in Figure 8. This dynamic spectrum shows the motion state of plasma, including motion direction and velocity magnitude along the line of sight, at different time and different temperature. In this figure, it becomes convenient for us to identify the time frame and temperature range of hot upflows and cold downflows as well as their motion velocities. We can clearly distinguish the differences between two kinds of redshifts at the temperature of 0.3–1.0 MK and <0.3 MK,

i.e., cooling inside post-flare loops and condensation at footpoints. Besides the different locations of the two kinds of redshifts, there are other two primary differences: (1) the condensation occurred almost at the same time with the chromospheric evaporation, whereas the cooling is posterior to the evaporation, probably because it takes time for the evaporated plasma to rise into the corona and then cool down by heat conduction and radiative loss; (2) since the cooled plasma within the loops is driven by gravity and travels a long distance equal to the height of flare loops, its freefall speed would be naturally larger than the velocity of the downflows of denser plasmas that are caused by the imbalanced heat pressure at footpoints.

In addition, the reversal temperature between hot upflows and cold downflows inside flaring regions could be studied from the EVE plasma dynamic spectrum. A different reversal temperature would imply a different energy deposition height, rate, or duration driven by magnetic reconnection (Liu et al. 2009). The evaporation model in Fisher et al. (1985) predicts that the reversal temperature is below 1 MK. In our study of this flare case, the reversal occurs close to 1 MK, as shown in Figure 8, which is similar to the observations in Kamio et al. (2005) and Del Zanna et al. (2006). This result implies that the boundary between upflowing/downflowing plasma is located approximately at the lower corona or the upper TR. There are explicit velocity structures of hot upflows above 2 MK and cold downflows below 0.5 MK, but the intermediate state near the temperature boundary of 1 MK is still unclear and needs further study.

Finally, we apply the DEM method again to check the exact positions where the aforementioned dynamic processes took place. Figure 9 shows the evolutions of DEM distribution in two temperature ranges, 6–8 MK and 0.5–1.0 MK, corresponding to chromospheric evaporation and cooling inside post-flare loops, respectively. The temperature of condensation at footpoints is too low for the DEM analysis and therefore is unable to be shown in the DEM map. The thermal structure of
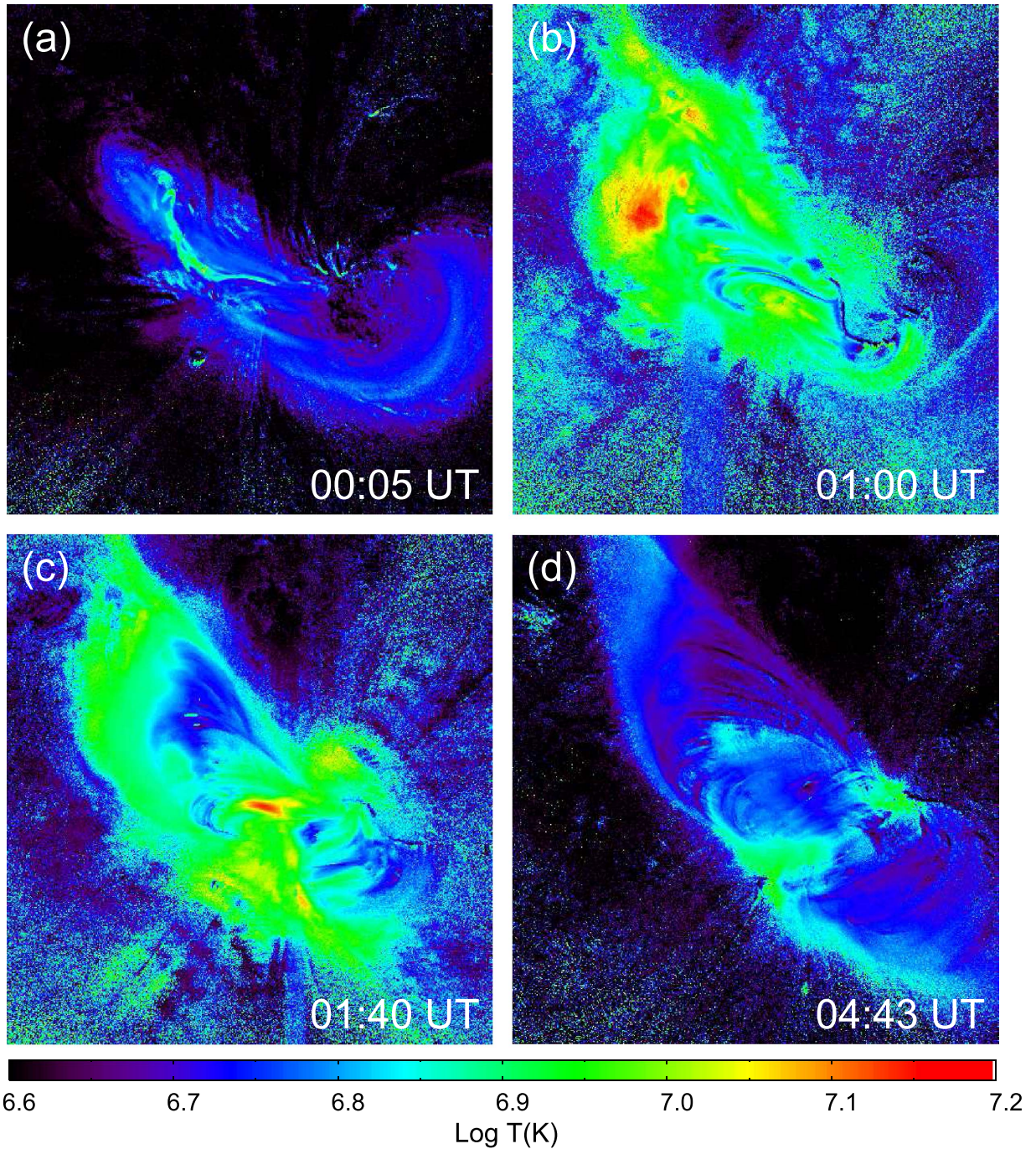
Figure 11. DEM temperature maps of the flare, showing the same region indicated by Figure 10. (a) At the flare onset (00:05 UT). (b) After the main peak. (c) and (d) After the second peak. The temperature range is 4–15 MK.

6–8 MK appeared at the north flare ribbon first (18:34 UT) and then moved upward along the leg of loops, conforming to the basic picture of chromospheric evaporation. We cannot see an obvious evolution of plasma emission on the other side because the south ribbon was covered by the huge post-flare loops. The emission from plasma at 0.5–1.0 MK showed an opposite direction of movement, enhancing first at the top of cool loops (18:30 UT) and subsequently expanding to the whole loop structure, which is consistent with the formation of the TR loops in AIA 171 images (see Figure 4). Such behavior of plasma emission indicates that there was some cold plasma moving from the top of loops to the feet, which is the cooling

process of evaporated plasma essentially. Basically, the DEM analysis agrees with the result from our spectroscopy study.

3.2. The X5.4 Flare on 2012 March 7

According to the *GOES* observation, the flare (N25W28) started at 00:05 UT and peaked at 00:24 UT, followed by a smaller peak in the gradual phase at 01:15 UT. Figure 10 shows the AIA 131 and 171 images at the flare onset, the main peak and the second small peak, displaying the formations of hot coronal loops and cool TR loops, respectively. Despite of the overexposure in the figure, large loops were found to be formed in the north at the main peak of the flare (00:24 UT) in both
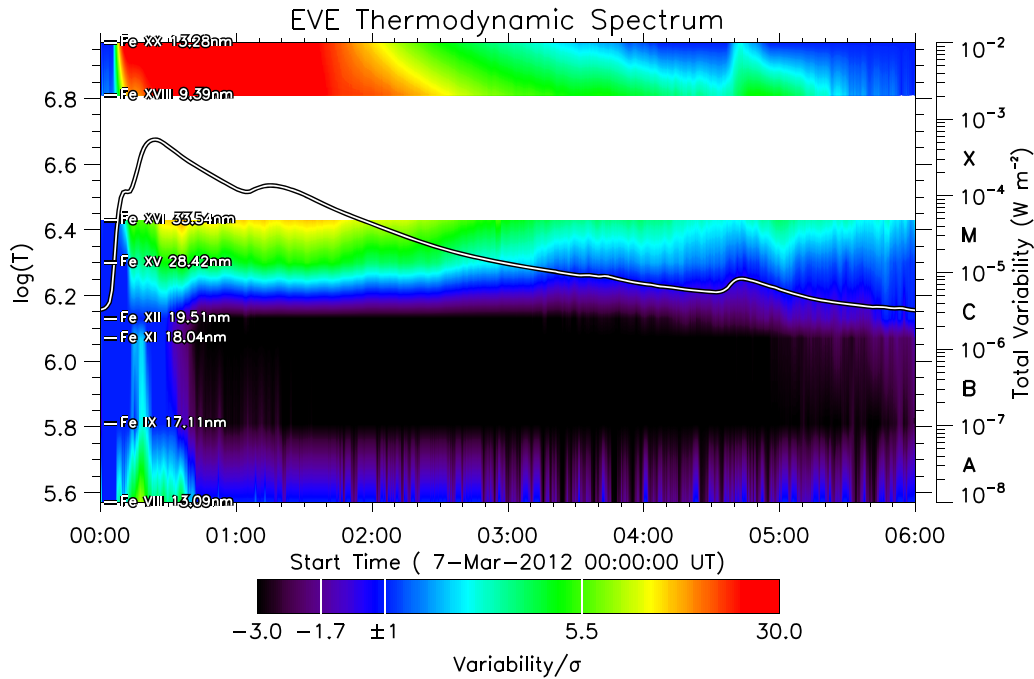
Figure 12. EVE thermodynamic spectrum chart showing the variability. The eight emission lines used in the charts are indicated on the left. The white line is derived from the *GOES* soft X-ray with the *y*-axis on the right.

AIA 131 and 171. Then, the subsequent brightening occurred at 01:15 UT and led to a series of relatively smaller loops in the south of the previous loops. Similar to the result in the first flare case, the cool loops in AIA 171 appeared at 01:42 UT, which is later than the hot ones in AIA 131 at 01:15 UT, suggesting a delayed cooling process in the TR. The time delay between the appearances of the hot and cool loops reaches about 30 minutes during the second peak of this flare.

The DEM temperature maps in Figure 11 show the evolution of the thermal structure of 4–15 MK in the corona. After the main peak of the flare (01:00 UT), the chromospheric evaporation led to the super-hot region at 15 MK close to the top of the north loops. Then, the south loops were heated and reached a temperature above 10 MK after the second peak (01:40 UT). Finally, the entire structure of the flare loops cooled down in the terminating phase of the flare (04:43 UT).

Figure 12 shows the EVE thermodynamic spectrum chart of the flare, lacking the three cold lines below 0.3 MK, because MEGS-B did not operate in this period. The emission of most EUV lines enhanced significantly in the impulsive phase. Then, the brightening of the coronal lines above 1 MK lasted for a long duration due to the second eruption of the flare, whereas the TR lines between 0.3 and 1 MK seemed to experience a dimming process in the gradual phase. In addition, the small X-ray peak at 04:43 UT was caused by another C-class flare in the visible solar disk.

The previous Doppler shift analysis is also applied to the seven emission lines from MEGS-A, and the result is shown in Figure 13. The moments of the flare onset, the main peak, and the second peak are indicated by the dashed lines in the figure. The chromospheric evaporation reflects in the blueshifts of Fe XVIII, Fe XVI, and Fe XV lines. Fe XVIII shows a strong blueshift of 202 km s^{-1}, which rapidly increased in the impulsive phase and lasted for about three hours, and Fe XVI and Fe XV present very slight blueshifts of 23 km s^{-1} and 25 km s^{-1}, respectively, in the gradual phase. It seems that the

main component of the evaporation has a temperature close to that of Fe XVIII line at 6.5 MK. Meanwhile, the redshift of Fe VIII line indicates the cold TR downflows in the gradual phase, with a delay of more than 10 minutes compared to the evaporation. The redshift of Fe VIII reached 172 km s^{-1} and lasted for nearly two hours. After the main peak of the flare, the second peak at 01:15 UT did not lead to an apparent change of the velocities of Fe XVIII, Fe XVI, Fe XV, and Fe VIII, probably because the plasma flows caused by the main peak had already reached a state of saturation when the second eruption occurred. In addition, there is still not a definite pattern of Doppler velocities of Fe IX, Fe XI, and Fe XII lines, which is the same as the first case.

Figure 14 shows the EVE plasma dynamic spectrum chart of this flare. Significant blueshifts above 2 MK and redshifts below 0.5 MK can be seen in the figure, corresponding to the upflows in chromospheric evaporation and downflows in cooling, respectively. The reversal temperature of upflowing/ downflowing plasma identified by the dynamic spectrum is close to 1 MK, where the plasma flows are inconspicuous, and the details of dynamic state inside the flaring region are not very explicit.

By comparing the observational results of the two X-class flares, we find that the dynamic and thermodynamic features of the EUV emission lines studied are basically consistent in many aspects.

4. Conclusion and Discussion

We studied two X-class flares on 2014 January 7 and 2012 March 7 by analyzing EVE data in a wide temperature range, from the lower TR to the flare corona. The EVE thermodynamic spectrum charts reveal the emission distribution of EUV lines against temperature and time and provide key information of flare thermodynamics. A typical thermal process of flares consists of intense coronal heating starting at the impulsive phase and subsequent cooling to the temperature of
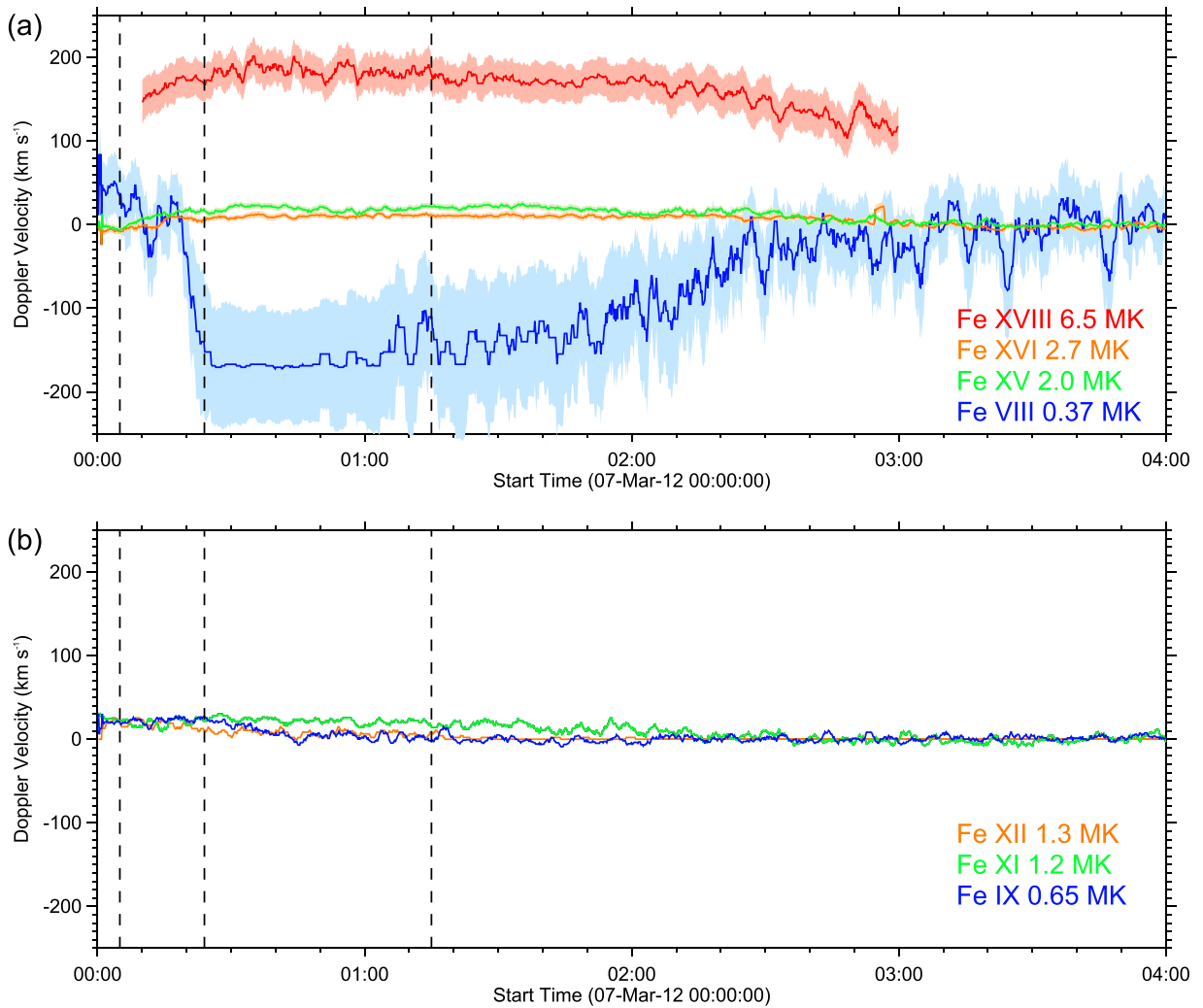
Figure 13. Doppler velocities of the seven emission lines from MEGS-A with positive/negative values corresponding to the blue/redshift. The uncertainties in the velocities are indicated by shadows, except for Fe XII, Fe XI, and Fe IX. The vertical dashed lines show the flare onset, the main peak, and the second peak, respectively.

TR. There are also some emission enhancements of lower TR lines in a short period after flare onset.

Based on the Doppler shift analyses of 10 EUV lines provided by EVE instrument, we construct 2D EVE plasma dynamic spectrum charts to observe various plasma flows inside flaring regions, comprehensively and conveniently. The dynamic spectrum provides a distribution of Doppler velocity in time-temperature map, and help us identify three kinds of plasma motion: chromospheric evaporation ($100–200 \, km \, s^{-1}$) above 1 MK, cooling downflows inside post-flare loops (approximately $150 \, km \, s^{-1}$) between 0.3 and 1 MK and condensation at footpoints ($<30 \, km \, s^{-1}$) below 0.3 MK. We find that the chromospheric evaporation and condensation both started just after the flare onset but the latter was only present within a short period in the impulsive phase, probably because the intense and rapid heating at footpoints diminished after the impulsive phase and the overpressure causing the condensation became faint. The cooling downflows inside the loops occurred after the above two processes in the gradual phase with a time delay of more than 10 minutes. The time delay gives a timescale of how the corona "consumes" the evaporation and the associated heat. AIA observations and DEM analyses consistently suggest that the cooled plasma moved downward

within the cold TR loops, from top to feet, which were below the hot coronal loops. Besides, the reversal temperature between blue/redshifts is close to 1 MK, implying that the boundary of upflowing/downflowing plasma is located at the lower corona or upper the TR. Finally, we draw a sketch map in Figure 15 to give an overall picture of the above plasma motion.

A puzzling phenomenon in the EVE thermodynamic spectrum charts (see Figures 6 and 12) is that there seems to be a gap between hot component of coronal heating and the cold component of cooling in the TR. Specifically, Fe IX 17.11 nm, Fe XI 18.04 nm, and Fe XII 19.51 nm have nearly no intensity enhancement during flares and make the thermodynamic spectra incontinuous with a temperature gap between 0.65–1.3 MK. This kind of gap in thermodynamic spectrum charts is not only found in the two cases in this paper, but also in a number of flare events presented in Paper I. Woods et al. (2011) reported a similar result where intensities of some cool coronal lines do not increase apparently in the impulsive phase and even decrease in the gradual phase and found that such coronal dimming is highly correlated with coronal mass ejection (CME) events. If it is true, the gap of EUV emission
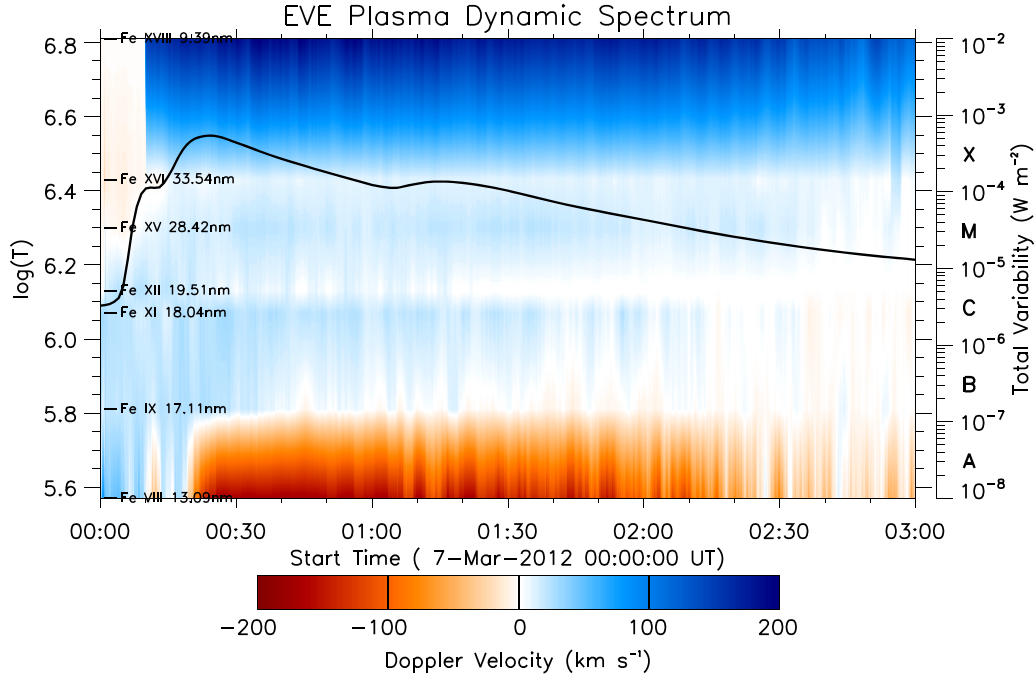
EVE Plasma Dynamic Spectrum

Figure 14. EVE plasma dynamic spectrum chart showing the Doppler shift. The seven emission lines used in the chart are indicated on the left. The black line is derived from the *GOES* soft X-ray with the *y*-axis on the right.
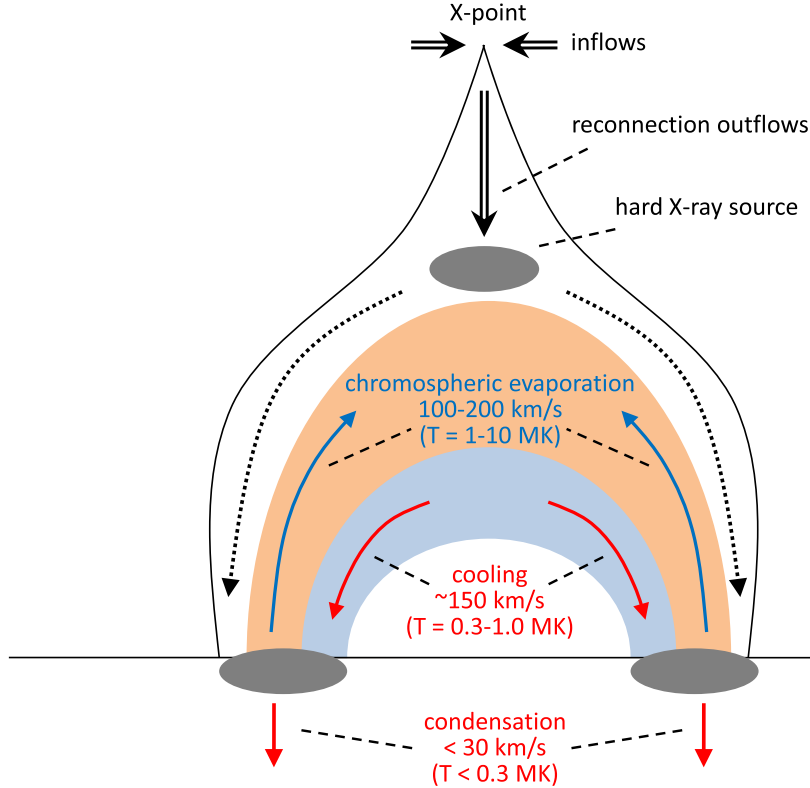

Figure 15. Sketch map of plasma motion in flare reconnection model, including hot upflows and cold downflows.

in the cool corona would be more obvious during eruptive flares.

We acknowledge use of data from the *SDO* and *GOES* spacecraft. *SDO* is a mission of NASA's Living With a Star Program. We are grateful to the anonymous referee for valuable and constructive comments. We thank Hui Tian from Peking University for valuable discussion. This work is supported by grants from the NSFC (41574165, 41761134088, 41774178, and 41421063) and the fundamental research funds for the central universities.

ORCID iDs

Zhixun Cheng ⓘ https://orcid.org/0000-0002-4020-3211
Yuming Wang ⓘ https://orcid.org/0000-0002-8887-3919
Rui Liu ⓘ https://orcid.org/0000-0003-4618-4979
Zhenjun Zhou ⓘ https://orcid.org/0000-0001-7276-3208
Kai Liu ⓘ https://orcid.org/0000-0003-2573-1531

References

Acton, L. W., Leibacher, J. W., Canfield, R. C., et al. 1982, ApJ, 263, 409
Bradshaw, S. J., & Cargill, P. J. 2005, A&A, 437, 311
Brosius, J. W., & Phillips, K. J. H. 2004, ApJ, 613, 580
Cheng, X., Zhang, J., Saar, S. H., & Ding, M. D. 2012, ApJ, 761, 62
Del Zanna, G., Berlicki, A., Schmieder, B., & Mason, H. E. 2006, SoPh, 234, 95
Dere, K. P., Landi, E., Mason, H. E., Fossi, B. C. M., & Young, P. R. 1997, A&AS, 125, 149
Dere, K. P., Landi, E., Young, P. R., et al. 2009, A&A, 498, 915
Emslie, A. G., Dennis, B. R., Shih, A. Y., et al. 2012, ApJ, 759, 71
Fisher, G. H. 1987, ApJ, 317, 502
Fisher, G. H., Canfield, R. C., & McClymont, A. N. 1985, ApJ, 289, 414
Fröhlich, C., & Lean, J. 2004, A&ARv, 12, 273
Graham, D. R., & Cauzzi, G. 2015, ApJL, 807, L22
Hirayama, T. 1974, SoPh, 34, 323
Hudson, H. S., Woods, T. N., Chamberlin, P. C., et al. 2011, SoPh, 273, 69
Kamio, S., Kurokawa, H., Brooks, D. H., Kitai, R., & UeNo, S. 2005, ApJ, 625, 1027
Li, Y., & Ding, M. D. 2011, ApJ, 727, 98
Li, Y., Ding, M. D., Qiu, J., & Cheng, J. X. 2015, ApJ, 811, 7
Liu, W., Petrosian, V., & Mariska, J. T. 2009, ApJ, 702, 1553
Milligan, R. O. 2008, ApJL, 680, L157
Moore, C. S., Chamberlin, P. C., & Hock, R. 2014, ApJ, 787, 32
Neupert, W. M. 1968, ApJL, 153, L59
Priest, E., & Forbes, T. 2001, A&ARv, 10, 313
Schmelz, J. T., Worley, B. T., Anderson, D. J., et al. 2011, ApJ, 739, 33
Schmieder, B., Heinzel, P., Wiik, J. E., et al. 1995, SoPh, 156, 337
Teriaca, L., Falchi, A., Cauzzi, G., et al. 2003, ApJ, 588, 596
Teriaca, L., Falchi, A., Falciani, R., Cauzzi, G., & Maltagliati, L. 2006, A&A, 455, 1123
Wang, Y., Zhou, Z., Zhang, J., et al. 2016, ApJS, 223, 4
Woods, T. N., Eparvier, F. G., Hock, R., et al. 2012, SoPh, 275, 115
Woods, T. N., Hock, R., Eparvier, F., et al. 2011, ApJ, 739, 59
Woods, T. N., Kopp, G., & Chamberlin, P. C. 2006, JGR, 111, A10S14